Astronomy & Astrophysics

Detection of frequency spacings in the young O-type binary HD 46149 from CoRoT photometry[*,**,***]

P. Degroote[1], M. Briquet[1,†], M. Auvergne[2], S. Simón-Díaz[3,4], C. Aerts[1,5], A. Noels[6], M. Rainer[7], M. Hareter[8], E. Poretti[7], L. Mahy[6], R. Oreiro[1], M. Vučković[1], K. Smolders[1,‡], A. Baglin[2], F. Baudin[9], C. Catala[2], E. Michel[2], and R. Samadi[2]

[1] Instituut voor Sterrenkunde, K.U.Leuven, Celestijnenlaan 200D, 3001 Leuven, Belgium
e-mail: pieter.degroote@ster.kuleuven.be
[2] LESIA, Observatoire de Paris, CNRS UMR 8109, Université Pierre et Marie Curie, Université Denis Diderot, 5 place J. Janssen, 92105 Meudon, France
[3] Instituto de Astrofísica de Canarias, 38200 La Laguna, Tenerife, Spain
[4] Departamento de Astrofísica, Universidad de La Laguna, 38205 La Laguna, Tenerife, Spain
[5] Department of Astrophysics, IMAPP, University of Nijmegen, PO Box 9010, 6500 GL Nijmegen, The Netherlands
[6] Institut d'Astrophysique et de Géophysique Université de Liège, Allée du 6 août 17, 4000 Liège, Belgium
[7] INAF – Osservatorio Astronomico di Brera, via E. Bianchi 46, 23807 Merate (LC), Italy
[8] Institut für Astronomie, Universität Wien Türkenschanzstrasse 17, 1180 Vienna, Austria
[9] Institut d'Astrophysique Spatiale, CNRS/Université Paris XI UMR 8617, 91405 Orsay, France

ABSTRACT

Aims. Using the CoRoT space based photometry of the O-type binary HD 46149, stellar atmospheric effects related to rotation can be separated from pulsations, because they leave distinct signatures in the light curve. This offers the possibility of characterising and exploiting any pulsations seismologically.
Methods. Combining high-quality space based photometry, multi-wavelength photometry, spectroscopy and constraints imposed by binarity and cluster membership, the detected pulsations in HD 46149 are analyzed and compared with those for a grid of stellar evolutionary models in a proof-of-concept approach.
Results. We present evidence of solar-like oscillations in a massive O-type star, and show that the observed frequency range and spacings are compatible with theoretical predictions. Thus, we unlock and confirm the strong potential of this seismically unexplored region in the HR diagram.

Key words. binaries: spectroscopic – stars: individual: HD 46149 – stars: massive – stars: oscillations – asteroseismology

1. Introduction

HD 46149 is a member of the young open cluster NGC 2244 in the heart of the Rosette Nebula, and one of the targets observed by the CoRoT satellite (Baglin et al. 2002), during the short run SRa02 as part of the asteroseismology programme (Michel et al. 2006). There is a general agreement about the spectral type of HD 46149: it is catalogued as an O8.5V star (e.g. Jaschek 1978; Walborn & Fitzpatrick 1990), an O8.5V((f))[1] (e.g. Massey et al. 1995) and as an O8V star (e.g. Keenan 1985; Mahy et al. 2009). The last authors also confirm that HD 46149 is actually a binary

system with a suspected hot B-type companion, although their dataset of radial velocity measurements did not suffice to determine the orbit. Conforming the expectations that a massive main sequence star of this type does not exhibit a strong stellar wind, Garmany et al. (1981) deduced a weak wind in the primary with a mass loss rate of $\log \dot{M} = -7.7 \pm 0.3$ from CIV resonance lines in IUE observations.

The known distance of 1.6 ± 0.2 kpc to the cluster and age estimate of 1–6 Myr (Bonatto & Bica 2009), makes this system a suitable candidate for asteroseismology. Moreover, we can assume that the chemical composition is similar to that of the cluster, effectively fixing the metallicity to $Z = 0.014$ with solar mixture (Asplund et al. 2005) and a hydrogen mass fraction of $X = 0.715$ (Przybilla et al. 2008). In the past, no serious attempts have been made to perform asteroseismological modelling of O stars owing to the lack of detected oscillations. This is primarily because the pulsation amplitudes are low, and there is possibly contamination by variable stellar winds. There is some observational evidence of pulsations in late O-type stars: spectroscopic line profile variations with amplitudes of $\sim$5 km s^{-1} have been detected and connected to nonradial pulsations in, e.g., ξ Persei and λ Cephei (de Jong et al. 1999). Also in photometry, variations have been detected and likely related to pulsation

---

[†] Postdoctoral Fellow of the Fund for Scientific Research, Flanders.
[‡] Aspirant Fellow of the Fund for Scientific Research, Flanders.
[1] The classification label ((f)) is given when strong HeII absorption and weak NIII emission is seen.

(e.g., Walker et al. 2005; Rauw et al. 2008). However, possible cyclical modulation of the wind makes the search for nonradial pulsations particularly troublesome, since the relevant frequency domains overlap. It is still an open question whether these mass outflows are connected to pulsations, to a nonhomogeneous magnetic field at the surface of the star (Hubrig et al. 2008), or to yet another phenomenon.

The low spectroscopic amplitudes translate to photometric amplitudes below mmag level, which is difficult to detect from the ground, but is within reach of CoRoT's high-precision space-based photometry. The high duty cycle is fit for monitoring full rotation cycles, capturing both the influence of the wind and pulsations.

In addition, a spectroscopic campaign has been set up involving 3 different telescopes, partially overlapping with the CoRoT observations and continuing over the months following the CoRoT run, to find clues to the open questions in the field of O-type star pulsations and stellar winds. The observations are summarised in Table A.1.

In the following sections, we use the grid of non-rotating stellar models computed by one of us (MB) with the evolutionary code CLÉS (Code Liégeois d'Évolution Stellaire, Scuflaire et al. 2008b), for interpretating the O9V star HD 46202. We used the OPAL2001 equation of state (Rogers & Nayfonov 2002; Caughlan & Fowler 1988), with nuclear reaction rates from Formicola et al. (2004) for the $^{14}N(p, \gamma)^{15}$ cross-section. Convective transport is treated by using the classical mixing length theory of convection (Böhm-Vitense 1958). For the chemical composition, we used the solar mixture from Asplund et al. (2005). We used OP opacity tables Seaton (2005) computed for this mixture. These tables are completed at $\log T < 4.1$ with the low-temperature tables of Ferguson et al. (2005). In the calculations, a static atmosphere and no mass loss were assumed.

We fixed the metallicity to $Z = 0.014$ and the hydrogen mass fraction to $X = 0.715$, according to the values derived for the cluster, and in agreement with the solar neighbourhood (Przybilla et al. 2008). We considered a mass range between 20 and 28 $M_\odot$ in steps of 0.1 $M_\odot$ and overshoot parameters $\alpha_{ov} = 0.0$–0.5 pressure scale heights in steps of 0.05. To better match the observed binary system, the grid was extended to 35 $M_\odot$ in steps of 0.5 $M_\odot$ and an overshoot parameter of $\alpha_{ov} = 0.2$.

Afterwards, for each main-sequence stellar model, we calculated the theoretical frequency spectrum of low-order p- and g-modes with a degree of the oscillation up to $\ell = 4$ using a standard adiabatic code for non-rotating stellar models (Scuflaire et al. 2008a). In Sect. 2, we use the CoRoT light curve to analyse the long- and short-period variability. In Sect. 3 we use the spectra to characterise the binary system to determine the fundamental parameters of the components, and end with a remark on the absence of spectroscopic variability.

Given all observational constraints, we finally interpret the short- and long-period variations in the CoRoT light curve in Sect. 4 in terms of rotation and stochastically excited pulsations, respectively.

2. The CoRoT data

2.1. Frequency analysis

The CoRoT satellite observed HD 46149 from 2 454 748.48856 HJD for 34 days with a sampling rate of 32 s (Fig. 1). In the frequency spectrum of the reduced light curve[2], we still see some

---

[2] N2 level data available at http://idoc-corot.ias.u-psud.fr
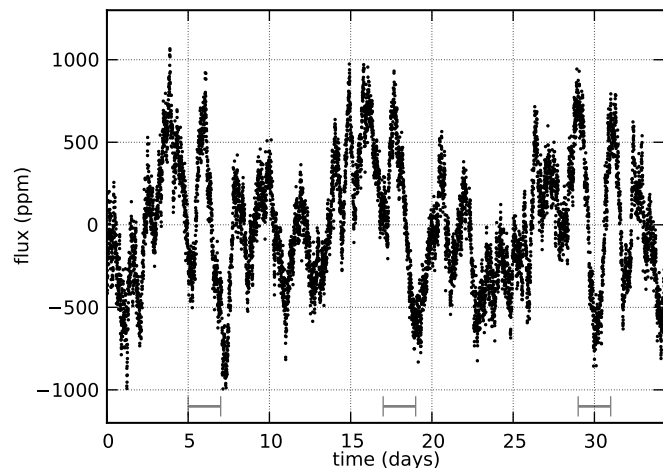
Fig. 1. Light curve of HD 46149 from CoRoT space based photometry, binned per 10 observations. The times of occurrence of the features causing the highest amplitude variation are indicated in grey ($t_0 = 2\,454\,748.48856$ HJD).

instrumental effects, and distinguish the large-amplitude, low-frequency signal from the low-amplitude high-frequency signal. In the following, we first remove most of the instrumental signal. Then, the low-frequency signal is separated from the high-frequency signal to analyse them separately, mainly focusing on the latter.

All flagged observations in the light curve were removed. The decreasing trend in the CoRoT light curve was removed by dividing by a linear fit, since it is visible in almost all CoRoT targets and is thus considered to be of instrumental origin (Auvergne et al. 2009).

The SAA crossing is a semiperiodic event and causes the strongest aliasing effect in the Fourier window, at $\approx 13.97\,\mathrm{d}^{-1}$. This is coupled to a semiperiodic dip in the light curve at the same position, introducing an artefact that is related both to sampling and flux variations. Because of the semiperiodic nature of the event, it is difficult to completely remove it from the light curve. However, since the nonharmonic signal with nearly constant frequency is heavily confined to specific bandwidths at regular intervals, we minimised the effect by first converting the light curve to Fourier space by iterative linear prewhitening, and then removing all signals related to frequencies outside the interval $13.97 \pm 0.05\,\mathrm{d}^{-1}$. We assumed that the remainder of the signal is only due to the orbit of the satellite, and removed that signal by fitting a 50th order spline of 3rd degree to the phasediagram of the dominant frequency, determined with the phase dispersion minimization procedure (Stellingwerf 1978) to account for the highly non-sinusoidal form of the signal. The parameters for the spline fit were fixed empirically, to optimally capture the discontinuity with a relatively low number of knot points. The raw Fourier periodogram with the orbital influence still present, the orbit model, and Fourier periodogram of the cleaned signal are shown in Fig. 2.

On the fully reduced light curve, we performed a traditional iterative prewhitening procedure (see, e.g., Degroote et al. 2009a). Because the first phase diagram has a non-sinusoidal shape, we did not perform a nonlinear fitting procedure using the inadequate sum-of-sines model. Instead, we used the Fourier decomposition to filter out specific bandwidths, between 0 and $0.2\,\mathrm{d}^{-1}$, 0.2 and $1.0\,\mathrm{d}^{-1}$, and 1.0 and $13\,\mathrm{d}^{-1}$ (regions a, b, c in Fig. 2). A common feature of the isolated signal from these
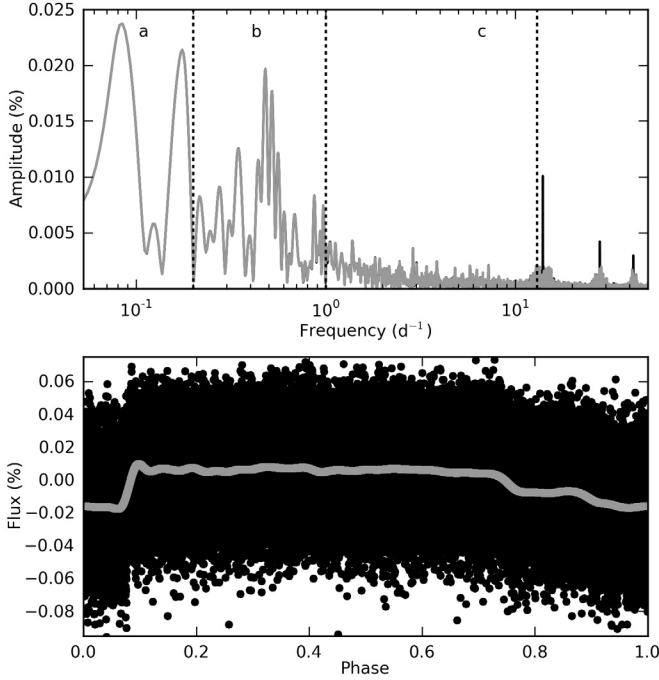
Fig. 2. (*Top panel*) Fourier periodogram of the CoRoT light curve of HD 46149, with the global trend removed (black) and with additional filtering of the satellite's orbital influences (grey). The black line is only visible where the grey and black lines do not overlap. The vertical dashed lines indicate the three different regions (a, b, c) in which stellar signal is detected. (*Bottom panel*) The residual CoRoT light curve where only the signal from the satellite is retained, folded on the satellite's orbital frequency ($\approx 13.97\,\mathrm{d}^{-1}$). The solid grey line represents the spline model for the instrumental signal.

regions is their self similarity: the autocorrelation of the low-frequency region reaches the 75% level at $\Delta t_l = 11.76 \pm 0.96\,\mathrm{d}$, the mid-frequency region shows a similar pattern when folded on this period (although the autocorrelation attains a maximum at $2\Delta t_l$), and a similar period is recovered in the highest peak in the autocorrelation of the high-frequency signal ($\Delta t_h = 11.5 \pm 0.1\,\mathrm{d}$) although at much lower amplitude (36%). The resemblance is confirmed by eye from the phase folded light curves with $P = 11.7\,\mathrm{d}$ (Fig. 3).
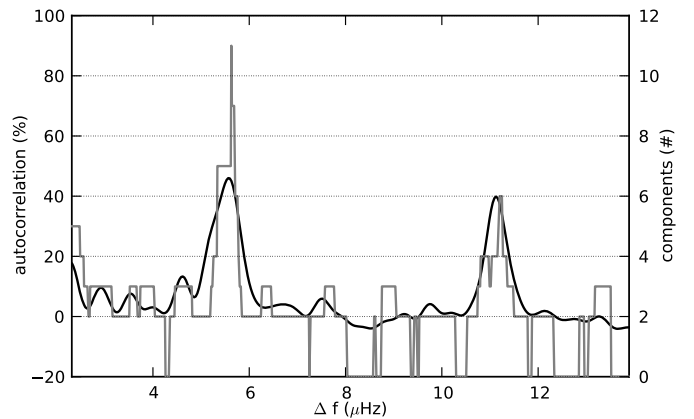
2.2. The frequency spacing

After prewhitening the long period signal below $3\,\mathrm{d}^{-1}$, a prominent frequency spacing is detected in the high-frequency regime. The limit of $3\,\mathrm{d}^{-1}$ is chosen because no dominant higher frequency peaks exist that can contaminate the lower amplitude peaks. Both the autocorrelation of the periodogram and spacing detection algorithms (Degroote et al. 2009b) uncover a spacing of $\Delta f = 0.48 \pm 0.02\,\mathrm{d}^{-1}$, where at least 12 individual members of the spacing can be recovered in the original linear frequency analysis (Fig. 4).

Fourier transformations of selected pieces of the light curve are unable to reproduce the values of the amplitudes. Specifically, a short-time Fourier transformation is not able to trace any of the frequencies throughout the entire light curve, and the emerging pattern suggests a stochastic nature for the modes (Fig. 5). Since the frequency resolution is high enough to adequately separate the different components, this implies that the modes are excited and damped, bearing a resemblance to *solar p-modes* (Baudin et al. 1994). Under such conditions, the mode
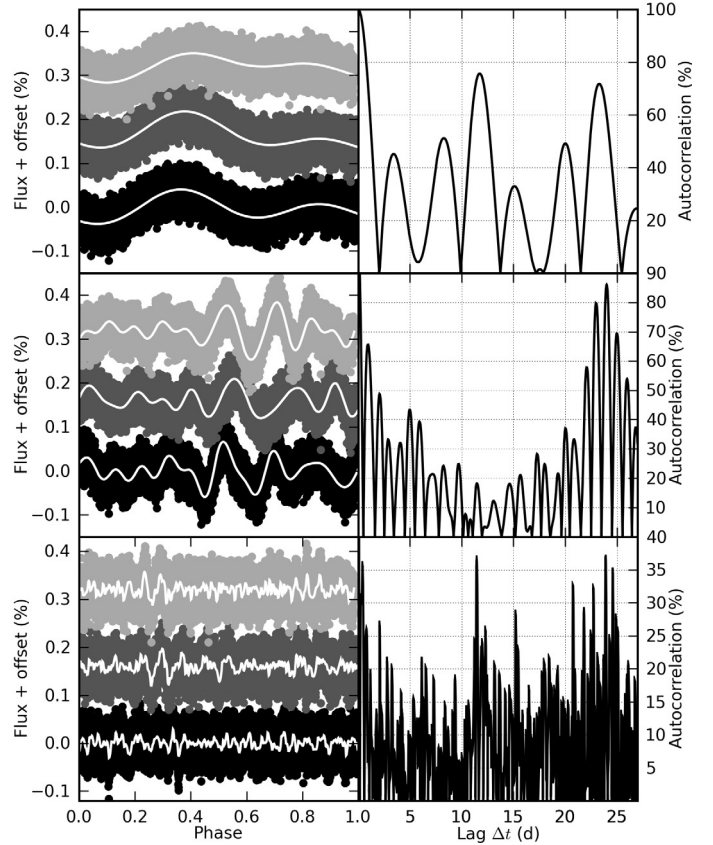
Fig. 3. (*Left panels*) CoRoT light curves folded on the period $P = 11.7\,\mathrm{d}$, where all the signal outside three adjacent passbands is removed (defined in Fig. 2). Consecutive phases are stacked on top of each other with increasing offset, and shown in consecutive shades of grey. (*Top to bottom*) Low-frequency signal, mid-frequency signal, high-frequency signal. (*Right panels*) Autocorrelation functions of the filtered light curves in the corresponding left panel.

Fig. 4. Autocorrelation function of the periodogram of the light curve where all low and mid-frequency signals are removed (black solid line), and the number of components in a chain of corresponding frequency spacing Δf (grey line).

lifetime can be estimated by fitting Lorentzian profiles simultaneously to N peaks in the power density spectrum $P(f)$ (e.g., Appourchaux et al. 1998; Carrier et al. 2010), via

$$P(f) = \sum_{n=1}^{N}\left(\frac{H_n}{1 + \left(\frac{2(f-f_n)^2}{\Gamma}\right)}\right) + B.$$
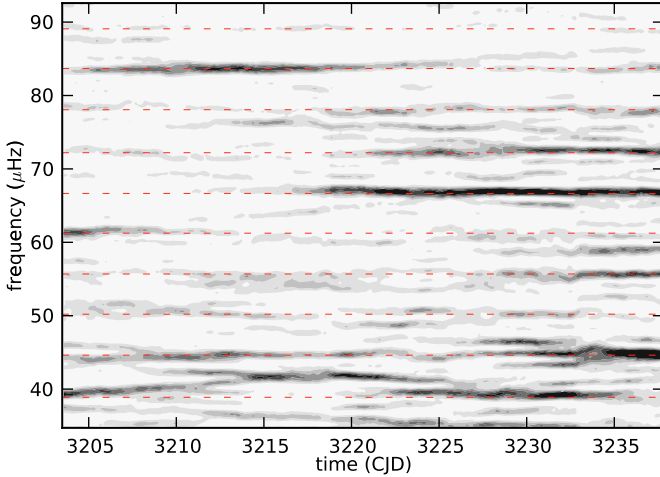
**Fig. 5.** Short time Fourier transformation (window width = 10 d) of the high-frequency region of the light curve, after filtering out the low- and mid-frequency regions. The different members of the frequency spacing identified from the complete light curve are indicated with red dashed lines, and show that the amplitudes connected to these frequencies vary significantly over the course of the time series ($t_0 = 2\,451\,545$ HJD).
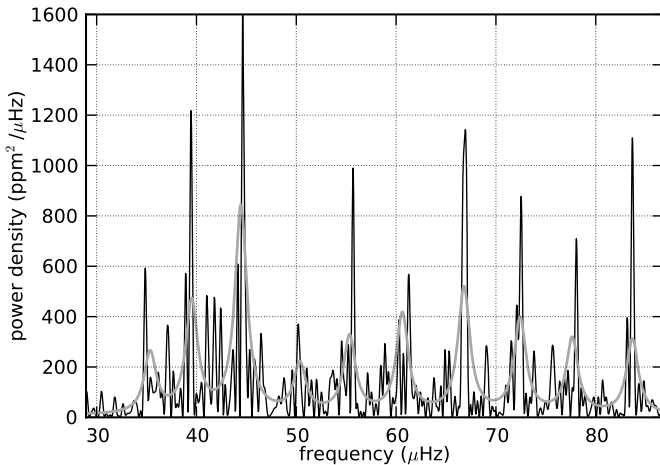
Fig. 6. Observed power spectrum (black line) and Lorentzian fit (grey line) with the same lifetime for all frequency peaks. The width of the Lorentzian profile implies a mode lifetime of the order of hours.

In this equation, H_n is the height of the profile of frequency f_n, B is the noise level, and Γ the mode line-width at half maximum. The power spectral density is obtained by multiplying the power spectrum with the total time span T. The fit is then performed by minimising

$$F = \ln P(f) + \frac{P(f)}{P_{\text{fit}}(f)},$$

using the Levenberg-Marquardt minimisation algorithm (Fig. 6). We decided to fix the mode lifetime to be equal for all the modes, reducing the number of parameters to fit, but removing the ability to constrain mode lifetimes individually. From the fit, we infer an average mode line width of $\Gamma = 1.05 \pm 0.15\,\mu$Hz corresponding to an average mode lifetime of $3.5^{+0.6}_{-0.4}$ days, which is consistent with the lifetime of the features in the short time Fourier transformations (Fig. 5). The fitted mode heights, amplitudes, and frequencies are listed in Table 1, where the mode amplitude $A_{\text{rms}} = \pi H \Gamma$. These amplitudes are not bolometric

Table 1. Parameters of Lorentzian fits to the frequency spectrum ($\Gamma = 1.05\,\mu$Hz).

f_n (μHz)	f_n (d^{-1})	H_n (ppm^2/μHz)	A_{rms} (ppm)
35.27 (0.15)	3.05	229 (38)	27.0 (2.9)
39.54 (0.12)	3.42	435 (66)	37.3 (4.0)
44.49 (0.11)	3.85	819 (102)	50.9 (3.9)
50.34 (0.15)	4.35	210 (61)	25.3 (3.3)
55.37 (0.09)	4.79	332 (68)	32.4 (3.0)
60.70 (0.16)	5.25	389 (66)	35.2 (3.0)
66.81 (0.06)	5.77	512 (67)	40.6 (2.9)
72.43 (0.08)	6.26	391 (67)	35.2 (2.9)
77.70 (0.15)	6.71	293 (49)	30.7 (2.9)
83.66 (0.04)	7.23	308 (36)	31.5 (2.7)

amplitudes but measured within the CoRoT bandpass (Michel et al. 2009).

The error estimates in Table 1 are derived using Monte Carlo simulations. Thousands of different realisations of the light curve were constructed by adding white Gaussian noise to the light curve after prewhitening the long period signal, where the standard deviation σ is determined as $\sigma = \sigma'/\sqrt{2}$, with σ' the standard deviation of light curve after differentiating every two consecutive points. Adding the extra noise to the original light curve results in an increase in the true noise level, making the error estimates conservative.

Since no spectroscopic or multi-colour mode identification is possible for any of the spaced frequencies, we cannot use the traditional forward modelling approach for low-degree modes (Ausseloos et al. 2004, e.g.) to compare theoretical models with the observations. Instead of fitting the frequency values separately, we use the method commonly adopted for solar-like oscillations, where we search for correspondence of both the value of the large frequency spacing, and the range of frequencies where the spacing occurs. Mode identification can then be done using the location of the ridges in the échelle diagram. In doing so, we want to establish a proof-of-concept, rather than full modelling of the stellar interior.

Before the observed spacing can be compared with stellar models, we have to constrain the star's fundamental parameters. Since we are dealing with a binary system for which no orbital constraints are given in the literature, we first concentrate on the binarity, to characterise the two components.

3. Orbital and fundamental parameters

3.1. Orbital parameters

To construct the radial velocity curve, we used the measurements from Mahy et al. (2009). They were obtained by averaging the fitted minimum of a Gaussian profile to the bottom halves of selected HeI lines from high-resolution spectra. To this set of observations, we added high-resolution spectra taken with the CORALIE ($R \approx 50\,000$, Baranne et al. 1996) and HERMES ($R \approx 85\,000$, Raskin & Van Winckel 2008) spectrographs on the 1.2 m twin telescopes Euler (La Silla, Chile) and Mercator (La Palma, Spain). Part of the CORALIE spectra were taken simultaneously with the CoRoT light curve. To account for the low signal-to-noise ratio in these spectra (S/N of ~60), the RV were obtained by two independent methods. First, we fitted Gaussian profiles to the HeI 4471 Å, HeI 5875 Å, OIII 5592 Å and SiIV 4088 Å absorption lines and considered the difference

of the Gaussian minimum and the rest wavelength[3] as a measure for the radial velocity. Because the upper part of some of these lines show a significant departure from a Gaussian profile (because of blending or additional broadening mechanisms), we only used the lower part of the lines to fit the Gaussian profile. The exact cutoff depth C was determined from a trade-off between the reduced χ^2 of the fit and the number of points used in the fit via

$$S(C) = 1/N^2 \sum \frac{(O_i - F_i)^2}{\sigma^2},$$

where O_i and F_i are the observed and fitted spectrum below the normalised continuum level C, σ^2 is the variance, and a minimum in S was pursued. There are consistent offsets in the RV determination from the different lines of ~5 km s^{-1}.

Second, we computed the cross correlation function (CCF), using 8 absorption lines with a minimum below 90% of the continuum flux level between 4300 and 4800 Å, while removing the continuum to suppress the noise. Since we have no appropriate template spectrum, we used the first observed spectrum as a template, losing the ability to calibrate the RV in an absolute way. Instead, we compared the differences in RV estimated with both methods, and concluded that they were consistent with each other within ~5 km s^{-1}. As a final value for the RVs, we used the average of the estimations from the Gaussian line profiles, and adopted the spread as a measure for the error.

Next, 2 high-resolution spectra were added from the HARPS spectrograph on the La Silla 3.6 m telescope (Mayor et al. 2003), from which the RV were derived in the same manner as described above. Finally, we added the single radial velocity measurement from Underhill & Gilroy (1990), which was determined via a line-bisector method using a single absorption line.

Because the secondary component in HD 46149 is only marginally visible (Fig. 8), we first treated it as a single-lined binary. Therefore, we fitted the best Keplerian orbit to the single set of RVs with the generalised least-square method of Zechmeister & Kürster (2009), and improved them using a non-linear fitting algorithm (Press et al. 1988) (Fig. 7). The parameter estimations of this long-period, highly eccentric system are listed in the top part of Table 2. The errors on the parameters were estimated using three methods; (a) bootstrapping 1000 random samples from the observations, (b) comparing the fitted parameters with the values obtained via a weighted fit, where we artificially reduced the influence of the CORALIE and HERMES measurements, since they are high in number but have a narrow spread in time. The third method (c) was a Monte Carlo simulation, generating thousands of datasets from the observed values and their estimated uncertainties. Per parameter, the largest error estimate obtained by the three methods was adopted, and are listed in Table 2.

The mass function for single-lined spectroscopic binaries (Hilditch 2001) follows from the eccentricity, semi-amplitude, and period listed Table 2, and is equal to

$$f(M_1, M_2, i) = \frac{(M_2 \sin i)^3}{(M_1 + M_2)^2} = 0.96 \pm 0.06. \qquad (1)$$

Assuming an orbital plane perpendicular to the plane of the sky ($i = 90°$), and a lower limit on the mass of primary of $M_1 \geq 20 \, M_\odot$, we arrive at a lower limit on the mass of the secondary of $M_2 \geq 9.3 \, M_\odot$.

---

[3] Ralchenko, Yu., Kramida, A.E., Reader, J. and NIST ASD Team (2008). NIST Atomic Spectra Database. Available: http://physics.nist.gov/asd3. National Institute of Standards and Technology, Gaithersburg, MD.
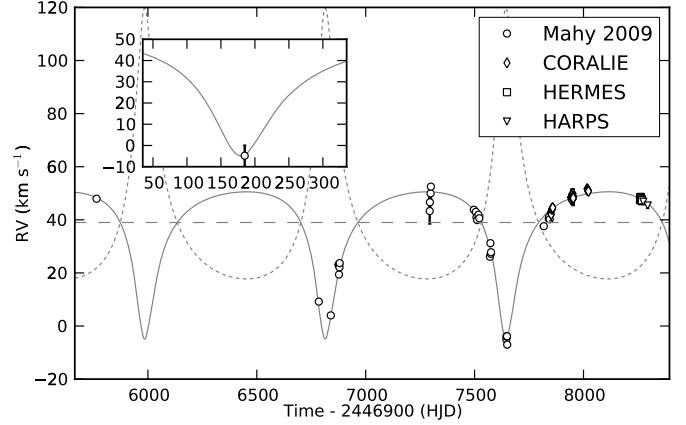

Fig. 7. Best Keplerian orbit fit (solid grey line) of the binary system HD 46149 based on archival RV measurements from Mahy et al. (2009), and on new CORALIE, HERMES, and HARPS spectra. The short dashed line represents the predicted orbit of the companion, corresponding to the spectroscopic fundamental parameters listed in Table 2. The long dashed grey line represents the mean radial velocity γ of the system. Inset is a zoom on the RV measurement of Underhill & Gilroy (1990), which was done ~15 years before the first measurement of Mahy et al. (2009).

3.2. Fundamental parameters

The spectral type of HD 46149 estimated by different authors ranges between O8V((f)) and O8.5V. For better establishing the stellar parameters of the primary component (and obtaining a rough estimation of the parameters of the secondary), we performed a spectroscopic analysis of the averaged CORALIE spectrum by means of the stellar atmosphere code FASTWIND (Puls et al. 2005), because these turned out to have the highest combined S/N. We applied the standard procedure in which a set of H and HeI-II lines in the optical spectra is fitted with synthetic lines from a grid of stellar atmosphere models created to this aim. In the averaging, binarity was taken into account by summing the profiles and assuming different luminosity ratios ($F_1/(F_1 + F_2) \in [0.5, 1]$). The projected equatorial rotation velocity $v_{\rm eq} \sin i = 30 \pm 10$ km s^{-1} of the primary was obtained by applying the Fourier transform method (Gray 1992, see also Simón-Díaz & Herrero (2007) for a recent application to OB-type stars) to the OIII 5592 Å line. The $v_{\rm eq} \sin i$ of the secondary was considered as a free parameter in the analysis. The parameters of the best fit and corresponding model parameters are listed in the top part of Table 2, where the uncertainties should not be strictly interpreted as the normal standard deviation, since many of the underlying distributions are skewed or are unknown. The spectroscopic solutions of both components lie on model isochrones, within the range expected from the age of the cluster (Fig. 11). In Fig. 8, the overall agreement is shown between the predicted and observed shape of the spectral lines.

Once the spectroscopic parameters are fixed, we can use the profiles to estimate the radial velocity of the companion, although the intrinsic uncertainty is high. In a spectrum from Mahy et al. (2009) taken at maximum velocity separation, we deduced an RV of ~110 km s^{-1}, which is compatible with the mass range deduced from the effective temperature and gravity from the spectroscopic fit (Fig. 7). Once the mass ranges of the two companions are fixed, we could deduce the inclination angle from Eq. (1), the semi-amplitude K_2 of the second component via $K_2 = (M_1/M_2)K_1$, and the semi-major axes from the
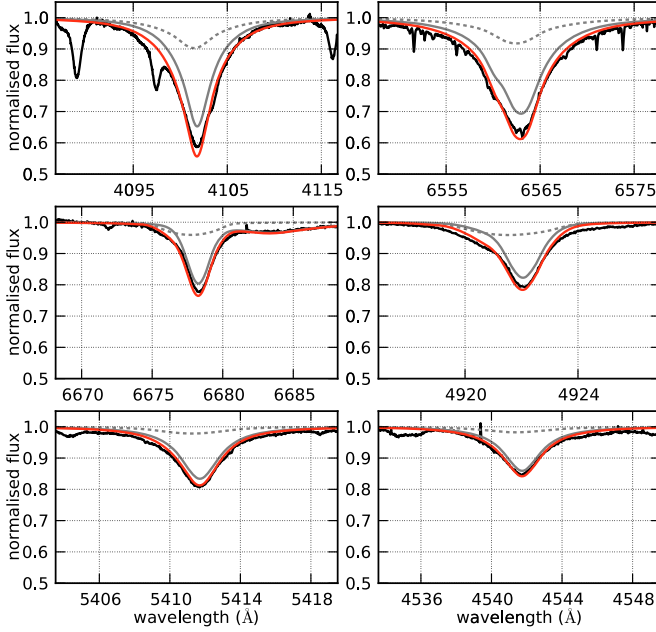
Fig. 8. Fits to the averaged CORALIE spectra (black). The parameters are listed in Table 2. The fit to the primary companion is shown in solid grey, the fit to the secondary in dashed grey, and the combined fit in red. The Hδ and Hα lines are most sensitive to the gravity, and Hα does not show any signs of a wind *(top panels)*. In the combined HeI 6678+HeII 6683 and HeI 4922 plots, the companion is clearly visible in the blue wing *(middle panels)*. The HeII 5410 and HeII 4541 are the most sensitive to the difference in temperatures of both components *(bottom panels)*.

estimates of $a_{1,2} \sin i$ (e.g., Hilditch 2001). These are listed in the second part of Table 2.

In the bottom part of Table 2, we also list the radii, luminosities, and masses, fullfilling both the spectroscopic fundamental parameters and the parameters of the computed grid of stellar models. Finally, we note a discrepancy between the spectral energy distribution (SED) of the system and the derived fundamental parameters (see Appendix B).

3.3. Spectroscopic variability

Besides a small emission feature at CIII 5696 Å (with an equivalent width of 22.5 ± 0.5 mÅ), there are no clear signs of emission in any of the spectra. We used three different methods to search for line profile variability in a selection of Si, O, He, and H lines: (a) we fitted a Gaussian profile to the lines and searched for variability in the moments (e.g., Aerts et al. 1992), (b) we calculated Fourier spectra per observed wavelength bin (e.g., Zima 2006), and (c) we constructed bisectors and searched for variability at different normalised flux levels (e.g., Gray 1992). Except for the radial velocity shift due to the binary orbit, no significant variability was detected.

4. Discussion

4.1. Origin of the low-frequency variability

The largest variations in the CoRoT light curve of HD 46149 take place on long time scales of days. Because of the relatively short time span of the observations, this unavoidably means those features are only seen for a few cycles, so are poorly

Table 2. Observed and corresponding model parameters.

Parameter	Value	Uncertainty
From spectroscopy		
P (d)	829	4
K_1 (km s^{-1})	27.7	0.4
e	0.59	0.02
Ω (°)	172.1	1.5
γ (km s^{-1})	39.0	0.3
T_0 (HJD)	2 454 538	5
$T_{\rm eff,1}$ (K)	36 000	1000
$T_{\rm eff,2}$ (K)	33 000	1500
$\log_{10} g_1$ (cgs)	3.7	0.1
$\log_{10} g_2$ (cgs)	4.0	0.15
$v_{\rm eq,1} \sin i$ (km s^{-1})	30	10
$L_1/L_{\rm tot}$	0.75	–
From binarity (and spectroscopic values)		
i (°)	49	9
a (AU)	6.5	0.1
K_2 (km s^{-1})	51	9
From CLÉS models (and spectroscopic values)		
$R_1 (R_\odot)$	13	2
$R_2 (R_\odot)$	7.5	2
$\log_{10} L_1 (L_\odot)$	5.4	0.2
$\log_{10} L_2 (L_\odot)$	4.8	0.2
$L_1/L_{\rm tot}$	0.80	0.20
$M_1 (M_\odot)$	35	6
$M_2 (M_\odot)$	19	3

resolved. In Table A.3, we list the amplitudes and frequencies of the most prominent peaks, with a *S/N* above 4, calculated over a 6 d^{-1} interval in the periodogram before prewhitening. The listed error estimates are formal errors, assuming isolated peaks. Most of them, however, are relatively close to each other ($\Delta f \sim 1/T = 0.03$ d^{-1}), making it difficult to draw conclusions on the individual peaks.

One possible way of interpreting the low frequency peaks is that they originate from g mode pulsations. However, the first frequency $f_1 = 0.08373$ d^{-1} is clearly nonsinusoidal, because the first harmonic ($f_2 = 0.17506$ d^{-1}) is also detected. From Fig. 3, we see that these two frequencies generate a pattern of two consecutive "bumps" with different amplitudes, which is not a typical pulsation signature (e.g., De Cat & Aerts 2002; De Cat et al. 2009). For a nonlinear mode, a distorted phase shape is expected. Also from Fig. 3, we see that the other high *S/N* peaks form a pattern that appears at fixed intervals in time, and vanish in between. The timescale between these patterns is similar to the period of f_1, $P = 11.76$ d. These considerations led us to conclude that the low-frequency signal is not likely to come from pulsations.

Another possible source of variability are atmospheric features, such as spots or chemically enhanced regions on the surface. The observed variability can then be explained by the appearance and disappearance of such features, either because of repeated creation and destruction or because of the rotation of the star. Here, we favour the second option, because of the signal's self-similarity, and because it is consistent with the spectroscopic determination of $v_{\rm eq} \sin i = 30 \pm 10$ km s^{-1}. With this assumption and an estimate of the radius $R = 13 \pm 2 R_\odot$ (see Table 2), we derive an inclination angle

$$i = \arcsin\left(\frac{v_{\rm eq} \sin i}{2\pi R \Omega}\right) \approx 32°,$$

with a lower limit of 20°. The ambiguity concerning the possibility that $2P$ is the true rotation period of the star is resolved by this argument, because no inclination angle is able to explain

such a low projected rotational velocity. We note the strong discrepancy up to a factor of two, with the projected rotational velocity of ~70 km s^{-1} from, e.g., Uesugi & Fukuda (1970). These authors assumed the whole broadening of the line profiles to be caused by rotation, while several studies have shown that this hypothesis may be incorrect in O and B stars (see, e.g., Ryans et al. 2002; Simón-Díaz & Herrero 2007). In contrast to previous estimations, we used the Fourier transform technique which, in principle, allows separating rotational broadening from other non-rotational broadenings in OB-type stars (Simón-Díaz & Herrero 2007).

An important source of spectroscopic line profile variations in O stars is cyclical wind variability (e.g., Henrichs et al. 2005). Due to having only one weak emission line (CIII 5696), which is thought to be formed by photospheric overpopulation (Leparskas & Marlborough 1979), and the absence of Hα emission, we deduce that HD 46149 has a very weak wind, in agreement with the result of Garmany et al. (1981). Although the S/N is too low to detect periodic variations in the spectra, there are faint hints that the wind is not constant. This is seen in the higher noise level of the amplitudes in the red wing of the hydrogen profiles than in the blue wing. In contrast, it is possible to detect the accumulated effect of all line profile variations in the broad-band integrated photometry performed by the CoRoT satellite. The predicted observed variation in the equivalent width of a specific spectral line to account for, e.g., a 0.02% amplitude in the light curve can be calculated as follows. First, a normalised observed spectrum is rescaled to a FASTWIND model atmosphere of $T_{\rm eff}$ = 35 000 K and $\log g$ = 4.0. Next, the calibrated spectrum is multiplied by the response curve of the CoRoT Asterochannel and normalised to have unit area. Finally, the equivalent line width variation of the model is predicted by rescaling the desired flux percentage to the normalised flux level. These calculations predict that an EW variation of 0.94 Å at 4000 Å, 0.67 Å at 5000 Å, and 1.14 Å at 6000 Å would separately all amount to a 0.02% integrated flux change. The influence on one specific line is much less, since the EW variation is spread over many lines. Given these numbers and the consideration that the flux continuum is also susceptible to variability, it is no surprise that we were unable to detect variability in the sparse timeseries of low S/N spectra.
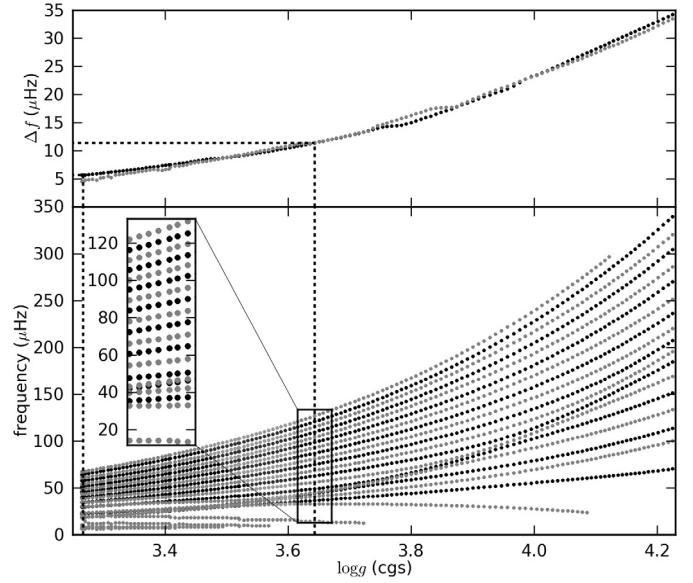
4.2. The frequency spacing

From the échelle diagram (Fig. 10), we can see the similarity with stochastically excited solar-like oscillations in low-mass stars, which are interpreted as pressure modes in the asymptotic frequency regime. From an initial extrapolation of the scaling law of Kjeldsen & Bedding (1995), the observed separation of Δf = 0.48 d^{-1} (or 5.5 μHz) is too small to be the large separation, and too large to be the small separation. To investigate this discrepancy further, we used the grid of stellar evolution models.

Starting from the list of adiabatic frequencies for these models, we searched for frequency spacings in the ℓ = 0, 1 modes between Δf = 0.2 d^{-1} (2.3 μHz) and Δf = 3 d^{-1} (34.7 μHz), where a small deviation of 0.1 d^{-1} was allowed from exact equidistance. We noticed that the extrapolated predicted frequency spacing from Kjeldsen & Bedding (1995),

$$\Delta f = 134.9 \sqrt{\frac{M}{R^3}} \, \mu\text{Hz},$$

is only valid for models near the terminal-age main sequence (TAMS) where the spacing value is low. The model grid used in


Fig. 9. *Lower panel*: Evolution of the adiabatic eigenfrequencies of a 30 $M_\odot$ model during the main sequence (ℓ = 0 modes are plotted in black, ℓ = 1 in grey). *Upper panel*: the value of the median frequency spacing. Dashed lines represent the frequency spacing Δf = 0.48 d^{-1} and $2\Delta f$. Inset is a zoom on the region compatible with the spectroscopic determination of the gravity.
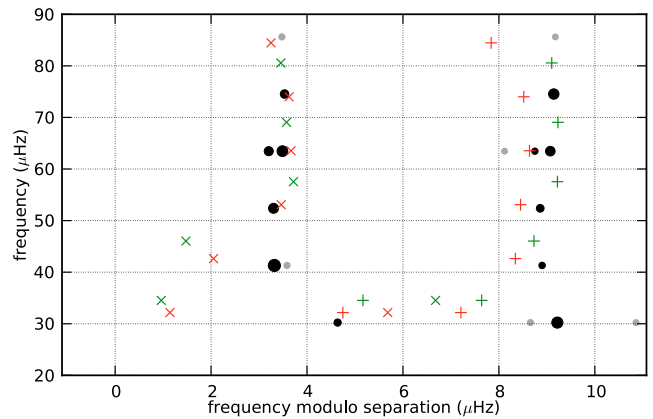
Fig. 10. Échelle diagram of observed frequencies (filled circles, the size of the dot scales with the power). Black circles represent modes with an amplitude above 11.5 ppm, the grey circles are modes with an amplitude above 10.5 ppm. The frequency values of ℓ = 0 ($\times$) and ℓ = 1 (+) modes are overplotted for the models of the primary component listed in Table 3 (red symbols denote the 30 $M_\odot$ model, green symbols denote the 34 $M_\odot$ model).

this paper, gives a slightly lower constant of proportionality of 120.4 ± 1.4 for massive stars above 20 $M_\odot$. We note, however, that the calculated frequencies are low-order p-modes ($n \le 10$), so the law of Kjeldsen & Bedding (1995) might not be applicable in this case.

From the spacing search analysis of the CLÉS models, we deduced that, for low-degree modes, Δf is above 3 d^{-1} at the zero-age main sequence, and gradually decreases to values around 1 d^{-1} and lower as the star evolves towards the TAMS, because of the increase in radius (Fig. 9). At the same time, the lower limit of the eigenfrequencies where the spacings occur, decreases from ~25 d^{-1} (290 μHz) to ~5 d^{-1} (58 μHz).
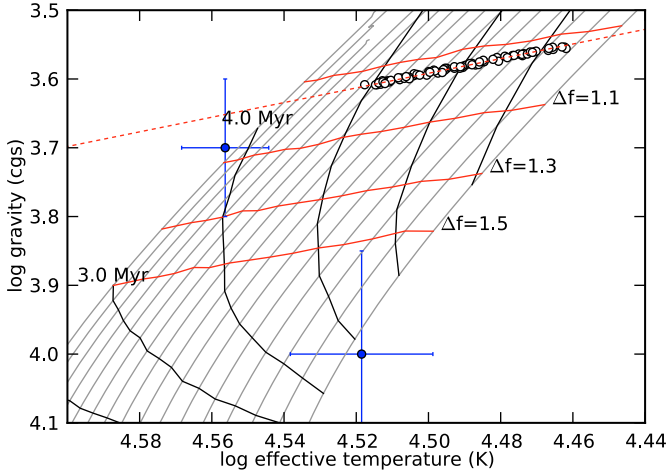
Fig. 11. log $T_{\rm eff}$-log g diagram of late O-type and early B-type stars. The spectroscopic parameter and corresponding error estimations of both components are indicated by the crosses. The evolutionary tracks (grey solid lines) are for masses of 20–35 $M_\odot$ and overshoot parameter $\alpha = 0.2$. The black solid lines denote the isochrones of 3–7 Myr. The horizontal solid red lines show the lines of constant density, and a large separation of $\Delta f = 1.0, 1.1, 1.3$ and 1.5. The open circles indicate the position of the models best fitting the observed spacing ($\Delta f = 0.98$). The red dashed line is a linear fit through these positions. Some models above 30 $M_\odot$ deviate from this fit, because the model grid is less dense in these regions.

We searched for the models in the grid for which both the spacing and the frequency values best match the observations. The best-fitting models were determined via a χ^2-like statistic,

$$S = \frac{1}{N} \sum_i (f_{i,\rm m} - f_{i,\rm o})^2,$$

where a minimum in S is searched for, resulting in those models where the average difference between the model frequencies and observed frequencies is minimal. From the location of the best-fitting models in the log $T_{\rm eff}$-log g diagram (Fig. 11), we inferred that they are located on a line of almost constant density, in agreement with what is known from the theory of stellar oscillations. We assumed that the observed spacing is half of the large separation between $\ell = 0$ modes (and thus the separation between $\ell = 0$ and $\ell = 1$) which is observed: a large separation of Δf would mean the star is at the end of the main sequence (Fig. 9), which is incompatible with spectroscopy. Thus, we assumed $\Delta f_{0,1} = 0.48\,\rm d^{-1}$. From this analysis, we inferred the following relation between the effective temperature and gravity for models with the observed spacing:

$$\log g = -1.20 + 1.06 \log T_{\rm eff}.$$

Using the observed $T_{\rm eff} = 36\,000 \pm 1000\,\rm K$, the latter fit predicts a gravity of log $g = 3.63 \pm 0.02$ (cgs), which is compatible with the observed value of log $g = 3.7 \pm 0.1$ (cgs) of the primary component of HD 46149. We compared the calculated frequency spectrum of two models for the primary on the log $g - T_{\rm eff}$ line defined above, with the observed frequency spectrum in Fig. 10. The parameters of the models are listed in Table 3. Overall, there is good agreement between the location of the ridges at high frequency, although the frequency values do not fit well individually. At lower frequencies, the observed frequencies deviate significantly from the model frequencies. We attribute this to the fact that, in the models, the spacing only appears above $\sim 50\,\mu$Hz

Table 3. Two representative models with overshoot parameter $\alpha = 0.2$ for the primary component of HD 46149, which show the observed spacing between the $\ell = 0, 1$ modes.

$M/M_\odot$	log $T_{\rm eff}$	log g	$R/R_\odot$	log $L/L_\odot$	Age (Myr)
30	4.512	3.575	14.80	5.341	5.0
34	4.539	3.643	14.56	5.436	4.2

(Fig. 9), making the low frequencies more sensitive to other parameters than the global mean density. In a future, more in-depth study of the pulsational characteristics of HD 46149, the discrepancies between the observed and theoretical frequency values should be accounted for. The lowest frequencies in the spacing could add additional constraints on the model physics.

5. Conclusions

We discovered modes with a finite lifetime in a massive O star binary system, for which we determined the orbital parameters, and constrained the fundamental parameters of both components spectroscopically. We removed the large-scale photometric variations, which we argued are due to changing features in the stellar atmosphere compatible with the rotational cycle of the star, instead of pulsations. The exact origin of this variability is unknown, but could be attributed to spots, stellar winds, or chemical inhomogeneities. After removing of these features, we interpreted the remaining signal as low-order pressure modes with a finite lifetime. Similar modes have been claimed before in the massive β Cephei star HD 180642 by Belkacem et al. (2009), and were interpreted as solar-like oscillations, excited by the convective region induced by the iron opacity bump (Belkacem et al. 2010). In the case of HD 46149, the frequency separation is compatible with the characteristic spacing between $\ell = 0, 1$ modes in stellar models. The observed spacing led to a mean density of the star, which is in good agreement with the parameters of the system derived from spectroscopy.

In a follow-up study, in-depth seismic modelling of this very massive binary will be considered by computing a fine but extensive grid of stellar models with various choices of the input physics, to try and fine-tune the physics for the most massive stars. Our observational results constitute a suitable starting point for in-depth seismic modelling of this very massive binary.

Appendix A: Tables

Table A.1 contains a list of the spectroscopic observations. The first column shows the time of observation, the second column the instrument used, and the third and fourth columns the exposure time and S/N, respectively.

Table A.1. Logbook of spectroscopic observations.

Time (HJD-2 450 000)	Instrument	Exp. time (s)	$\langle S/N \rangle$
4748.77151	CORALIE	1800	45
4750.80021	CORALIE	1800	56
4751.79249	CORALIE	1800	25
4753.83953	CORALIE	1800	62
4755.86699	CORALIE	1800	69
4756.75304	CORALIE	1800	57
4758.76337	CORALIE	1500	61
4842.59491	CORALIE	1800	64
4842.67488	CORALIE	1800	64
4842.75034	CORALIE	1800	61
4843.58534	CORALIE	1800	65
4843.64708	CORALIE	1800	62
4843.79525	CORALIE	1800	60
4844.62333	CORALIE	1800	63
4844.70675	CORALIE	1800	64
4845.59027	CORALIE	1800	56
4845.77435	CORALIE	1800	51
4846.58948	CORALIE	1801	64
4846.68792	CORALIE	1801	66
4846.74996	CORALIE	1801	64
4847.58828	CORALIE	1801	64
4847.68662	CORALIE	1801	60
4848.61953	CORALIE	1800	60
4848.69951	CORALIE	1800	62
4850.61492	CORALIE	1800	59
4850.67672	CORALIE	1800	59
4851.59201	CORALIE	1800	57
4852.56425	CORALIE	1800	49
4852.62809	CORALIE	1800	60
4852.73125	CORALIE	1800	58
4912.55844	CORALIE	1800	59
4916.51655	CORALIE	1800	60
4918.54146	CORALIE	1801	58
4920.55779	CORALIE	1801	59
4922.55891	CORALIE	1801	57
5159.72850	HERMES	420	27
5160.47824	HERMES	1200	65
5162.53878	HERMES	800	63
5162.54759	HERMES	600	57
5162.77441	HERMES	800	64
5162.78425	HERMES	800	60
5167.68048	HERMES	900	45
5167.69148	HERMES	900	44
5167.78661	HERMES	1200	54
5174.68443	HARPS	620	141
5194.66678	HARPS	800	169

Table A.2. Literature photometry of HD 46149.

Wavelength (Å)	System	Band	Reference
900–1150	FUSE	Far-UV	Sahnow et al. (2000)
1150–3300	IUE	UV	Boggess et al. (1978)
2740	TD1	UV	Boksenberg et al. (1973)
3641	JOHNSON	U	Johnson (1965)
4448	JOHNSON	B	Johnson (1965)
5504	JOHNSON	V	Johnson (1965)
12 487	JOHNSON	J	Johnson (1965)
16 464	JOHNSON	H	Johnson (1965)
21 951	JOHNSON	K	Johnson (1965)
4204	TYCHO	BT	Perryman & ESA (1997)
5321	TYCHO	VT	Perryman & ESA (1997)
4718	SDSS	g	Abazajian et al. (2004)
6185	SDSS	r	Abazajian et al. (2004)
7499	SDSS	i	Abazajian et al. (2004)
8961	SDSS	z	Abazajian et al. (2004)
7885	COUSINS	I	Cousins (1976)
12 412	2MASS	J	Cutri et al. (2003)
16 497	2MASS	H	Cutri et al. (2003)
21 909	2MASS	K_S	Cutri et al. (2003)
35 375	IRAC	36 μm	Fazio et al. (2004)
44 750	IRAC	45 μm	Fazio et al. (2004)
57 019	IRAC	58 μm	Fazio et al. (2004)
77 843	IRAC	80 μm	Fazio et al. (2004)
87 973	MSX	A	Egan et al. (2003)

Table A.3. List of high *S/N* frequency peaks.

A (ppm)	$\sigma(A)$	$f\,(\mu\mathrm{Hz})$	$\sigma(f)$	*S/N*
240.6	1.9	0.9691	0.0015	12.27
199.6	1.8	2.0262	0.0015	11.91
201.8	1.6	5.5546	0.0016	11.12
163.1	1.5	6.0215	0.0017	10.33
131.2	1.5	4.0575	0.0020	9.12
96.0	1.4	0.5159	0.0030	6.22
81.3	1.4	10.075	0.0032	6.01
85.0	1.4	6.4911	0.0030	6.34
88.6	1.3	5.1096	0.0031	6.37
83.5	1.3	7.9442	0.0030	6.61
63.9	1.3	11.2296	0.0035	5.87
64.3	1.3	1.7303	0.0037	5.75
57.0	1.2	3.6946	0.0044	4.93
52.8	1.2	2.9027	0.0046	4.71
47.0	1.2	3.2964	0.0050	4.50
51.7	1.2	12.1920	0.0050	4.57
41.7	1.2	7.0373	0.0053	4.38
49.0	1.2	15.9927	0.0056	4.24
33.6	1.2	10.8596	0.0059	4.04
36.6	1.2	33.4241	0.0060	4.01
19.0	1.1	83.6793	0.0106	4.17

Table A.2 lists the literature photometry. The first column denotes the wavelength range or average wavelength of the response function. The second and third columns denote the photometric system and the name of filter. The last columns contain references to the catalogues used or instruments.

Table A.3 is a list of all high *S/N* frequency peaks with their respective amplitudes. The *S/N* is computed by dividing the amplitude through the average noise level in the periodogram over a 6 d^{-1} interval in the periodogram.

Appendix B: Spectral energy distribution

The SED of the system can be used as an independent test for the derived fundamental parameters in Sect. 3.2. Some uncertainty is introduced, however, because the Balmer discontinuity is located in the far UV part of the spectrum, which is potentially heavily distorted due to extinction effects. Still, many flux measurements are found in the literature in a broad spectral range (Table A.2), which can be used to infer that there is little or no dust surrounding HD 46149, since no significant infrared excess is observed (Fig. B.1). The SED also delivers an independent measure for the radius of the primary component, assuming a radius ratio of both components, via

$$F_{\mathrm{obs}}(\lambda) = \left(F_{\mathrm{mod},1}(\lambda) + F_{\mathrm{mod},2}(\lambda)\frac{R_2^2}{R_1^2} \right) \frac{R_1^2}{d^2} E(\lambda).$$

A FASTWIND (Puls et al. 2005) grid of model atmospheres was used to provide the basic stellar flux models. The predicted fluxes $F_{\mathrm{mod},1,2}(\lambda)$ were computed by interpolating the grid to the values obtained from spectroscopy (Table 2), and the factor
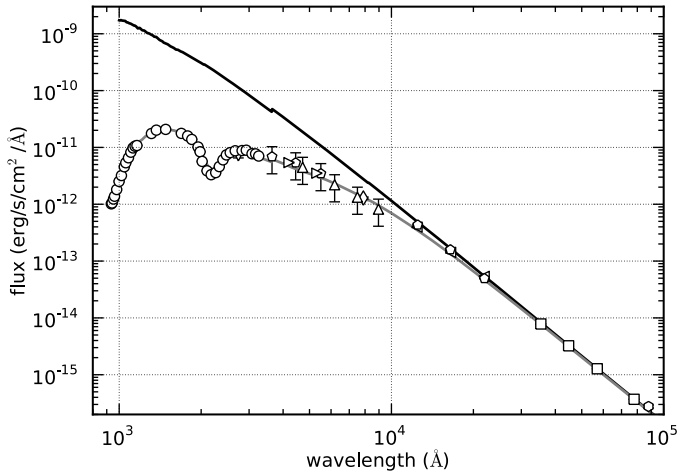
R_2^2/R_1^2 was also adopted from Table 2. A grid search was performed to find the minimum values of wavelength-dependent extinction $E(\lambda)$ (Cardelli et al. 1989) and R_1^2/d^2 in the following way: all values between $E(B-V) = 0$ and $E(B-V) = 2$ with a stepsize of 0.1 are adopted, and the search is iterated in a smaller interval around the minimum value until convergence is reached (i.e., until two consecutive minima differ less than 0.001 from each other). From the known distance to the system of $d = 1.6 \pm 0.2$ kpc and fitted extinction $E(B-V) = 0.46 \pm 0.05$ in agreement with literature values, we derive the following relation between R_1 and d:

$$R_1[R_\odot] = 5.13d \text{ [kpc]}.$$

Thus we arrive at an estimate of the radius of $R_1 = 8.3 \pm 2 R_\odot$, assuming the radius ratio of 0.6 from Table 2. This is lower than the one obtained from confronting models with the spectroscopic fundamental parameters. On the other hand, fixing the radius of the primary to the value in Table 2, leads to overestimating the distance compared to the literature value. Such discrepancies between different methods of parameter estimations have been reported before (e.g., Herrero et al. 1992).

References

Abazajian, K., Adelman-McCarthy, J. K., Agüeros, M. A., et al. 2004, AJ, 128, 502
Aerts, C., de Pauw, M., & Waelkens, C. 1992, A&A, 266, 294
Appourchaux, T., Gizon, L., & Rabello-Soares, M. 1998, A&AS, 132, 107
Asplund, M., Grevesse, N., Sauval, A. J., Allende Prieto, C., & Blomme, R. 2005, A&A, 431, 693
Ausseloos, M., Scuflaire, R., Thoul, A., & Aerts, C. 2004, MNRAS, 355, 352
Auvergne, M., Bodin, P., Boisnard, L., et al. 2009, A&A, 506, 411
Baglin, A., Auvergne, M., Barge, P., et al. 2002, in Stellar Structure and Habitable Planet Finding, ed. B. Battrick, F. Favata, I. W. Roxburgh, & D. Galadi, ESA SP, 485, 17
Baranne, A., Queloz, D., Mayor, M., et al. 1996, A&AS, 119, 373
Baudin, F., Gabriel, A., & Gibert, D. 1994, A&A, 285, L29
Belkacem, K., Samadi, R., Goupil, M.-J., et al. 2009, Science, 324, 1540
Belkacem, K., Dupret, M. A., & Noels, A. 2010, A&A, 510, A6
Boggess, A., Carr, F. A., Evans, D. C., et al. 1978, Nature, 275, 372
Böhm-Vitense, E. 1958, Z. Astrophys., 46, 108
Boksenberg, A., Evans, R. G., Fowler, R. G., et al. 1973, MNRAS, 163, 291
Bonatto, C., & Bica, E. 2009, MNRAS, 394, 2127
Cardelli, J. A., Clayton, G. C., & Mathis, J. S. 1989, ApJ, 345, 245
Carrier, F., De Ridder, J., Baudin, F., et al. 2010, A&A, 509, A73
Caughlan, G. R., & Fowler, W. A. 1988, Atom. Data Nucl. Data Tables, 40, 283
Cousins, A. W. J. 1976, MmRAS, 81, 25
Cutri, R. M., Skrutskie, M. F., van Dyk, S., et al. 2003, 2MASS All Sky Catalog of point sources., ed. R. M. Cutri, M. F. Skrutskie, S. van Dyk, et al.
De Cat, P., & Aerts, C. 2002, A&A, 393, 965
De Cat, P., Wright, D. J., Pollard, K. R., et al. 2009, in AIP Conf. Ser. 1170, ed. J. A. Guzik, & P. A. Bradley, 483
de Jong, J. A., Henrichs, H. F., Schrijvers, C., et al. 1999, A&A, 345, 172
Degroote, P., Aerts, C., Ollivier, M., et al. 2009a, A&A, 506, 471
Degroote, P., Briquet, M., Catala, C., et al. 2009b, A&A, 506, 111
Egan, M. P., Price, S. D., Kraemer, K. E., et al. 2003, VizieR Online Data Catalog, 5114, 0
Fazio, G. G., Hora, J. L., Allen, L. E., et al. 2004, ApJS, 154, 10
Ferguson, J. W., Alexander, D. R., Allard, F., et al. 2005, ApJ, 623, 585
Formicola, A., Imbriani, G., Costantini, H., et al. 2004, Phys. Lett. B, 591, 61
Garmany, C. D., Olson, G. L., van Steenberg, M. E., & Conti, P. S. 1981, ApJ, 250, 660
Gray, D. F. 1992, The observation and analysis of stellar photospheres, ed. Gray, D. F.
Henrichs, H. F., Schnerr, R. S., & Ten Kulve, E. 2005, in The Nature and Evolution of Disks Around Hot Stars, ed. R. Ignace, & K. G. Gayley, ASP Conf. Ser., 337, 114
Herrero, A., Kudritzki, R., Vilchez, J. M., et al. 1992, in Lecture Notes in Physics, The Atmospheres of Early-Type Stars, ed. U. Heber, & C. S. Jeffery (Berlin: Springer Verlag), 401, 21
Hilditch, R. W. 2001, An Introduction to Close Binary Stars, ed. R. W. Hilditch
Hubrig, S., Schöller, M., Schnerr, R. S., et al. 2008, A&A, 490, 793
Jaschek, M. 1978, Bull. Information du Centre de Données Stellaires, 15, 121
Johnson, H. L. 1965, ApJ, 141, 923
Keenan, P. C. 1985, in Calibration of Fundamental Stellar Quantities, ed. D. S. Hayes, L. E. Pasinetti, & A. G. D. Philip, IAU Symp., 111, 121
Kjeldsen, H., & Bedding, T. R. 1995, A&A, 293, 87
Leparskas, H. J. A., & Marlborough, J. M. 1979, PASP, 91, 101
Mahy, L., Nazé, Y., Rauw, G., et al. 2009, A&A, 502, 937
Massey, P., Johnson, K. E., & Degioia-Eastwood, K. 1995, ApJ, 454, 151
Mayor, M., Pepe, F., Queloz, D., et al. 2003, The Messenger, 114, 20
Michel, E., Baglin, A., Auvergne, M., et al. 2006, in ESA SP 1306, ed. M. Fridlund, A. Baglin, J. Lochard, & L. Conroy, 39
Michel, E., Samadi, R., Baudin, F., et al. 2009, A&A, 495, 979
Perryman, M. A. C., & ESA, eds. 1997, The HIPPARCOS and TYCHO catalogues. Astrometric and photometric star catalogues derived from the ESA HIPPARCOS Space Astrometry Mission, ESA SP, 1200
Press, W., Flannery, B., Teukolsky, S., & Vetterling, W. 1988, Numerical Recipes in C (Cambridge: Press Syndicate of the University of Cambridge)
Przybilla, N., Nieva, M., & Butler, K. 2008, ApJ, 688, L103
Puls, J., Urbaneja, M. A., Venero, R., et al. 2005, A&A, 435, 669
Raskin, G., & Van Winckel, H. 2008, in SPIE Conf. Ser., 7014
Rauw, G., De Becker, M., van Winckel, H., et al. 2008, A&A, 487, 659
Rogers, F. J., & Nayfonov, A. 2002, ApJ, 576, 1064
Ryans, R. S. I., Dufton, P. L., Rolleston, W. R. J., et al. 2002, MNRAS, 336, 577
Sahnow, D. J., Moos, H. W., Ake, T. B., et al. 2000, ApJ, 538, L7
Scuflaire, R., Montalbán, J., Théado, S., et al. 2008a, Ap&SS, 316, 149
Scuflaire, R., Théado, S., Montalbán, J., et al. 2008b, Ap&SS, 316, 83
Seaton, M. J. 2005, MNRAS, 362, L1
Simón-Díaz, S., & Herrero, A. 2007, A&A, 468, 1063
Stellingwerf, R. F. 1978, ApJ, 224, 953
Uesugi, A., & Fukuda, I. 1970, Catalogue of rotational velocities of the stars, ed. A. Uesugi, & I. Fukuda
Underhill, A. B., & Gilroy, K. K. 1990, ApJ, 364, 626
Walborn, N. R., & Fitzpatrick, E. L. 1990, PASP, 102, 379
Walker, G. A. H., Kuschnig, R., Matthews, J. M., et al. 2005, ApJ, 623, L145
Zechmeister, M., & Kürster, M. 2009, A&A, 496, 577
Zima, W. 2006, A&A, 455, 227